CELL BIOLOGY

Bacterial gasdermins reveal an ancient mechanism of cell death

Alex G. Johnson[1,2]†, Tanita Wein[3]†, Megan L. Mayer[4], Brianna Duncan-Lowey[1,2], Erez Yirmiya[3], Yaara Oppenheimer-Shaanan[3], Gil Amitai[3], Rotem Sorek[3]*, Philip J. Kranzusch[1,2,5]*

Gasdermin proteins form large membrane pores in human cells that release immune cytokines and induce lytic cell death. Gasdermin pore formation is triggered by caspase-mediated cleavage during inflammasome signaling and is critical for defense against pathogens and cancer. We discovered gasdermin homologs encoded in bacteria that defended against phages and executed cell death. Structures of bacterial gasdermins revealed a conserved pore-forming domain that was stabilized in the inactive state with a buried lipid modification. Bacterial gasdermins were activated by dedicated caspase-like proteases that catalyzed site-specific cleavage and the removal of an inhibitory C-terminal peptide. Release of autoinhibition induced the assembly of large and heterogeneous pores that disrupted membrane integrity. Thus, pyroptosis is an ancient form of regulated cell death shared between bacteria and animals.

In mammals, gasdermin proteins execute pyroptotic cell death by oligomerizing into membrane pores that release inflammatory cytokines and induce cell lysis. The human genome encodes six gasdermin proteins (GSDMA to GSDME and pejvakin), including the prototypical member GSDMD (*1*–*3*). Gasdermin activation requires caspase- or granzyme-mediated cleavage of an interdomain linker that liberates a lipophilic N-terminal domain (NTD) from a large inhibitory C-terminal domain (CTD) (*4*–*6*). Proteolysis enables gasdermin NTD oligomerization and the formation of membrane pores important for innate immunity in mammals and primitive eukaryotes (*7*–*9*). Recent structural analyses have explained a mechanism of gasdermin pore formation (*5*, *6*, *10*, *11*), but the evolutionary origin and biological roles of diverse gasdermin proteins remain unknown (*12*).

While analyzing bacterial antiphage defense islands, we identified uncharacterized genes with predicted homology to mammalian gasdermins (table S1). Sequence analysis revealed 50 bacterial gasdermins (bGSDMs) that form a clade distinct from that of eukaryotic homologs (Fig. 1A and fig. S1) (*7*, *9*, *13*). We determined crystal structures of bGSDMs from *Bradyrhizobium tropiciagri* and *Vitiosangium sp.*, which revealed that bGSDMs each adopt a shared overall architecture that exhibits notable homology to the mammalian gasdermin NTD (fig. S2B and table S2), including the conservation of a twisted central antiparallel β sheet and the shared placement of connecting helices and strands throughout the periphery (Fig. 1, B and C).

The structures revealed complete absence of the large α-helical CTD required to maintain mammalian gasdermins in an autoinhibited state (Fig. 1). Although lacking the CTD, the bGSDM structures adopted the same conformation as that of the inactive mammalian gasdermin complex (Fig. 1, B and C). In the inactive structure of mammalian GSDMA3, the NTD forms two interfaces with the CTD that mediate autoinhibition, with the primary interface at the α1 helix and the β1-β2 hairpin (Fig. 1C) (*5*, *11*). Cleavage of GSDMA3 results in NTD activation through the lengthening of strands β3, β5, β7, and β9 and oligomerization of ~27 protomers into a membrane-spanning pore (*2*, *5*, *6*). Both the *Bradyrhizobium* and *Vitiosangium* bGSDM structures contained strands equivalent to GSDMA3 β1 to β2 and β6 to β9, but in bGSDMs, a short C-terminal peptide wrapped around the twisted β sheet core and terminated across strand β2 to stabilize the inactivated state (Fig. 1, B and C).

While building the bGSDM atomic models, we observed a snakelike density protruding from the *Bradyrhizobium* cysteine C3 sidechain. The density occupies a hydrophobic tunnel across the protein that is capped by F25 from the C-terminal peptide. In the 1.5-Å *Bradyrhizobium* bGSDM electron density map, the density could be assigned as a 16-carbon palmitoyl thioester (Fig. 1D and fig. S2C). We confirmed bGSDM palmitoylation with mass spectrometry and found that a cysteine at this position is conserved in gasdermins across most bacteria and some fungi (Fig. 1A and fig. S3, A and B). The presence of the palmitoyl in a hydrophobic cavity suggests that bGSDM palmitoylation occurs through autocatalysis (*14*). Palmitoylation contributes to stability of the inactive state protein (Fig. 1E), and modeling suggests substantial reorganization of residues along the hydrophobic tunnel during bGSDM activation (Fig. 1D and fig. S2, C and D) (*6*).

The majority of bGSDMs (43 of 50) are genomically encoded next to one or more genes with a predicted protease domain (Fig. 2A; fig. S5, A to C; and table S1). In most cases, the associated proteases are caspase-like peptidases, including peptidase C14 (Pfam database ID PF00656) and CHAT (Pfam ID PF12770) proteases (Fig. 2B and fig. S5A). Fungal gasdermins are also commonly encoded next to protease domain–containing genes (40 of 52) (table S3 and fig. S5B) and are activated through proteolysis (*13*). bGSDM-protease systems are found in diverse bacteria and archaea, as well as in metagenomic samples of prokaryotic origin (fig. S5D and table S4). Analysis of the bGSDM-associated proteases revealed that they are fused to divergent repeat or NACHT domains frequently involved in pathogen recognition and inflammasome function in human innate immunity (Fig. 2B and fig. S5C) (*15*). bGSDM genes are occasionally encoded near known immune defense systems (Fig. 2A, fig. S7A, and tables S1 and S4), so we tested bGSDM systems for a role in antiphage defense. bGSDM systems evolutionarily distant from the model organism *Escherichia coli* exhibited no discernible phage restriction (fig. S6). However, a four-gene operon from *Lysobacter enzymogenes* exhibited robust defense against coliphages T4, T5, and T6 (Fig. 2, C and D, and fig. S6, B and C). Deletion of the bGSDM gene from the *Lysobacter* operon abolished protection (Fig. 2, C and D, and fig. S6C). Thus, the bGSDM is essential for defense.

Expression of some of the bGSDM-protease systems in *E. coli* induced potent cellular toxicity in the absence of phage infection (Fig. 2, E and F; fig. S7, B and C; and table S5). Particularly strong toxicity was observed for a *Runella* system, which required bGSDM palmitoylation (Fig. 2E and fig. S7, B and C). Time-lapse microscopy in the presence of propidium iodide (PI) showed that cells expressing the *Runella* system ceased dividing and lost membrane integrity, which suggests that bGSDM activation induces membrane disruption (Fig. 2, E and F; fig. S7D; and movies S1 and S2). Mutation of the predicted *Runella* caspase-like protease active site residues H796 and C804 ablated all cellular toxicity (Fig. 3A). The *Runella* bGSDM and protease only induced cellular toxicity when expressed together, which suggests that the protease targets bGSDM during system activation (Fig. 3A and fig. S8A). In fact, a mutation that disrupted the active site of the second trypsin-like protease in the *Lysobacter* bGSDM system abolished antiphage defense (fig. S8B).

[1]Department of Microbiology, Harvard Medical School, Boston, MA 02115, USA. [2]Department of Cancer Immunology and Virology, Dana-Farber Cancer Institute, Boston, MA 02115, USA. [3]Department of Molecular Genetics, Weizmann Institute of Science, Rehovot 76100, Israel. [4]Harvard Center for Cryo-Electron Microscopy, Harvard Medical School, Boston, MA 02115, USA. [5]Parker Institute for Cancer Immunotherapy, Dana-Farber Cancer Institute, Boston, MA 02115, USA.
*Corresponding author. Email: philip_kranzusch@dfci.harvard.edu (P.J.K.); rotem.sorek@weizmann.ac.il (R.S.)
†These authors contributed equally to this work.

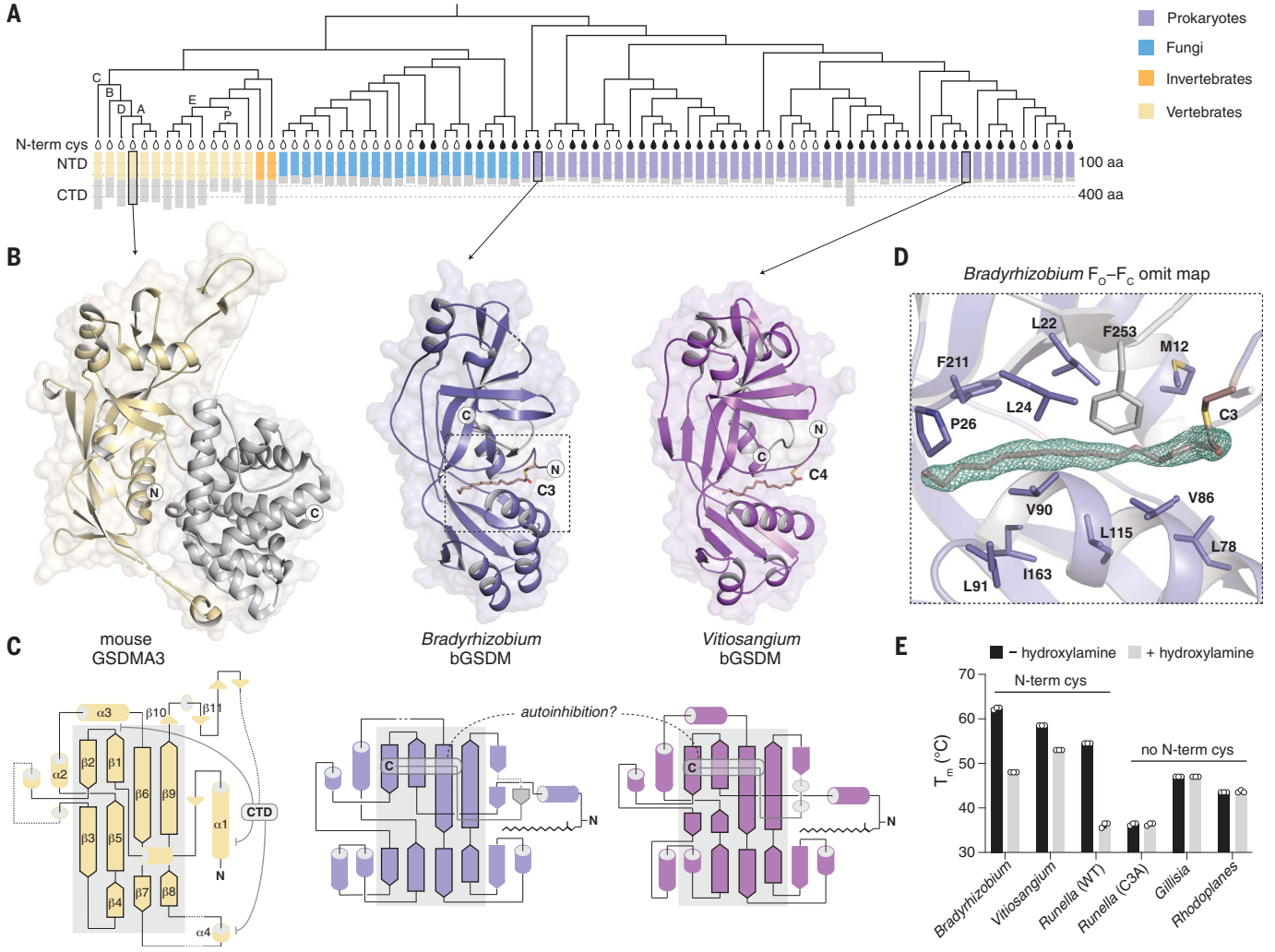

Fig. 1. Structures of bGSDMs reveal homology with mammalian cell death effectors. (**A**) Gasdermin phylogenetic tree. The sizes of the gasdermin NTDs and CTDs are depicted. Vertebrate gasdermins are labeled with single letters ("A" to "E") indicating human gasdermins GSDMA to GSDME, and "P" depicts pejvakin. The black teardrop indicates a conserved N-terminal cysteine (N-term cys). A representative set of 20 fungal gasdermins are included in the tree. aa, amino acid. (**B**) Crystal structures of bGSDMs from species of the genera *Bradyrhizobium* and *Vitiosangium*. bGSDM structures reveal homology to the NTD of mammalian gasdermins in an inactive conformation, including mouse GSDMA3 (Protein Data Bank ID 5B5R). (**C**) Gasdermin topology diagrams indicate a conserved central core of the bacterial and mammalian NTD. bGSDMs notably lack the CTD required for autoinhibition of mammalian gasdermins and instead encode a short C-terminal peptide. (**D**) Simulated annealing F_O–F_C omit map (contoured at 3.0 σ) from the *Bradyrhizobium* bGSDM fit with a palmitoyl modification at C3. Omit map is shown as green mesh, and select residues forming a hydrophobic pocket around the palmitoyl group are indicated. (**E**) Melting temperatures (T_m) of bGSDMs with and without N-terminal cysteines, as determined with thermofluor assays. Data are the means and standard deviations of three technical replicates and are representative of three independent experiments. WT, wild-type. Single-letter abbreviations for the amino acid residues are as follows: A, Ala; C, Cys; D, Asp; E, Glu; F, Phe; G, Gly; H, His; I, Ile; K, Lys; L, Leu; M, Met; N, Asn; P, Pro; Q, Gln; R, Arg; S, Ser; T, Thr; V, Val; W, Trp; and Y, Tyr.

We focused on the *Runella* system and reconstituted cleavage with purified components (Fig. 3B and fig. S8, A to F). Coincubation with the protease resulted in specific bGSDM cleavage and formation of a lower–molecular weight *Runella* bGSDM species (fig. S8A). Cleavage requires the protease catalytic residues but not bGSDM palmitoylation (Fig. 3B and fig. S8, D and E). Using mass spectrometry, we determined that the *Runella* bGSDM cleavage site occurs after the P1 residue L247 (fig. S9, A and B). A 2.9-Å structure of the *Runella* bGSDM (table S2) revealed that cleavage occurs in a loop that immediately precedes the C-terminal peptide (Fig. 3, C and D). Packing in the *Runella* bGSDM crystal lattice additionally indicates an ability of the peptide to dissociate from the bGSDM face, which supports release after cleavage (fig. S10A).

Analysis of the high-resolution *Bradyrhizobium* bGSDM structure explains how the C-terminal peptide restrains the bGSDM core (Fig. 3E). *Bradyrhizobium* bGSDM F245 and F247 lay along the surface formed between the mammalian β9 strand and the α1 helix equivalent positions and are further supported with contacts between N21 and the peptide backbone. A *Bradyrhizobium*-specific β strand from N21 to L24 extends off the β9 strand equivalent

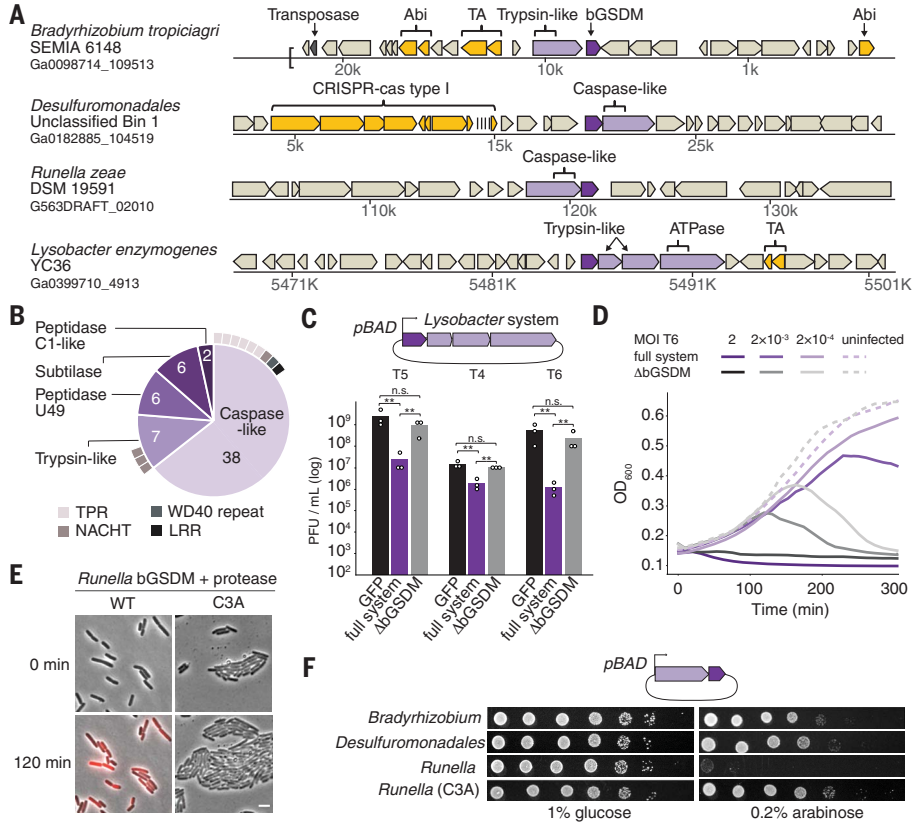

Fig. 2. bGSDMs are associated with proteases, defend from phages, and execute cell death. (**A**) Representative instances of bGSDMs and associated proteases in their genomic neighborhoods. Genes known to be involved in antiphage defense are shown in yellow. TA, toxin-antitoxin; Abi, abortive infection; ATPase, adenosine triphosphatase. (**B**) Types of proteases found adjacent to bGSDMs (n = 59). Some bGSDMs appear with more than one adjacent protease. Caspase-like proteases include peptidase C14 (n = 15) and CHAT (n = 23). Cases in which the protease gene also encodes an additional domain are indicated. TPR, tetratricopeptide repeat; LRR, leucine-rich repeat. (**C**) A bGSDM-containing operon protects against phages. The efficiency of plating of phages on *E. coli* MG1655 cells expressing the *Lysobacter* bGSDM WT or mutated operon is shown. Data represent plaque-forming units (PFU) per milliliter and are the averages of three independent replicates, with individual data points overlaid. GFP represents a control strain. Statistical significance was determined by a one-way analysis of variance (ANOVA) and Tukey multiple comparison test. Not significant (n.s.) ≥ 0.05; $^{**}P$ = 0.001 to 0.01. (**D**) Growth of liquid cultures of *E. coli* expressing the WT and mutated *Lysobacter* bGSDM operons. Cells were infected with phage T6. For each experiment, data represent one out of three biological replicates (replicates are shown in fig. S6). OD_{600}, optical density at 600 nm. (**E**) The *Runella* bGSDM operon causes cell death. *E. coli* DH5α cells expressing the *Runella* protease and WT or C3A-mutated bGSDM were examined by time-lapse microscopy. Overlay images from PI (red) and phase contrast of cells captured at the start of the experiment and after 120 min of incubation are shown. Scale bar, 2 μm. (**F**) bGSDM operons are toxic. Cells encoding protease and WT or mutated bGDSM were plated in 10-fold serial dilution on LB-agar in conditions that repress operon expression (1% glucose) or induce expression (0.2% arabinose).

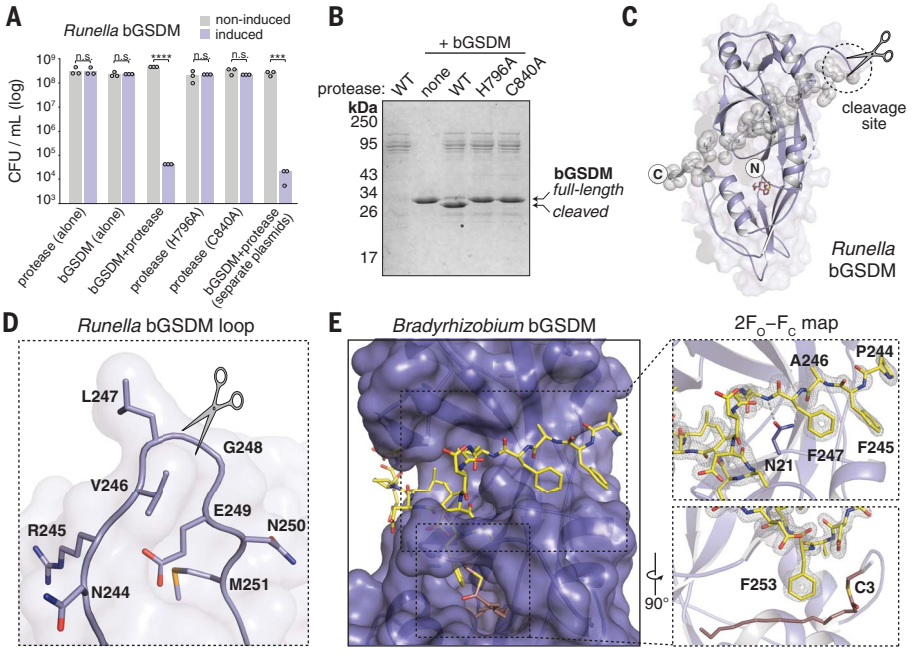

Fig. 3. bGSDMs are activated by proteolytic cleavage. (**A**) Toxicity of *Runella* bGSDM in vivo requires the associated protease. Bacteria expressing WT and mutated versions of the *Runella* bGSDM–protease operon were grown on LB-agar in conditions that repress or induce expression. Data represent colony-forming units (CFU) per milliliter, and bar graphs represent an average of three independent replicates, with individual data points overlaid. Asterisks indicate statistically significant differences compared with the respective noninduced control using two-sided t test. n.s. ≥ 0.05; $^{***}P$ = 0.0001 to 0.001; $^{****}P$ < 0.0001. (**B**) *Runella* bGSDM cleavage by its associated protease is dependent on catalytic histidine and cysteine residues in vitro. Fifteen percent SDS–polyacrylamide gel electrophoresis (SDS-PAGE) gels were run after cleavage at room temperature for 18 hours and visualized by Coomassie staining. (**C**) The *Runella* bGSDM crystal structure and protease cleavage site. The *Runella* bGSDM structure is shown in lavender with the last 21 amino acids highlighted as gray spheres. (**D**) Close-up view of the *Runella* bGSDM cleavage site wherein cleavage occurs after the P1 L247 residue. (**E**) Structural overview of the *Bradyrhizobium* CTD and autoinhibitory interactions. The bGSDM is colored purple except for its last 16 residues, which are colored yellow. Insets show interactions of F245 and F247 adjacent to D21 of the N-terminal β sheet (top) and F253 and the palmitoyl modification at C3 (bottom). The $2F_O–F_C$ (contoured at 1.5 σ) map is shown as gray mesh fit to the last 16 residues.

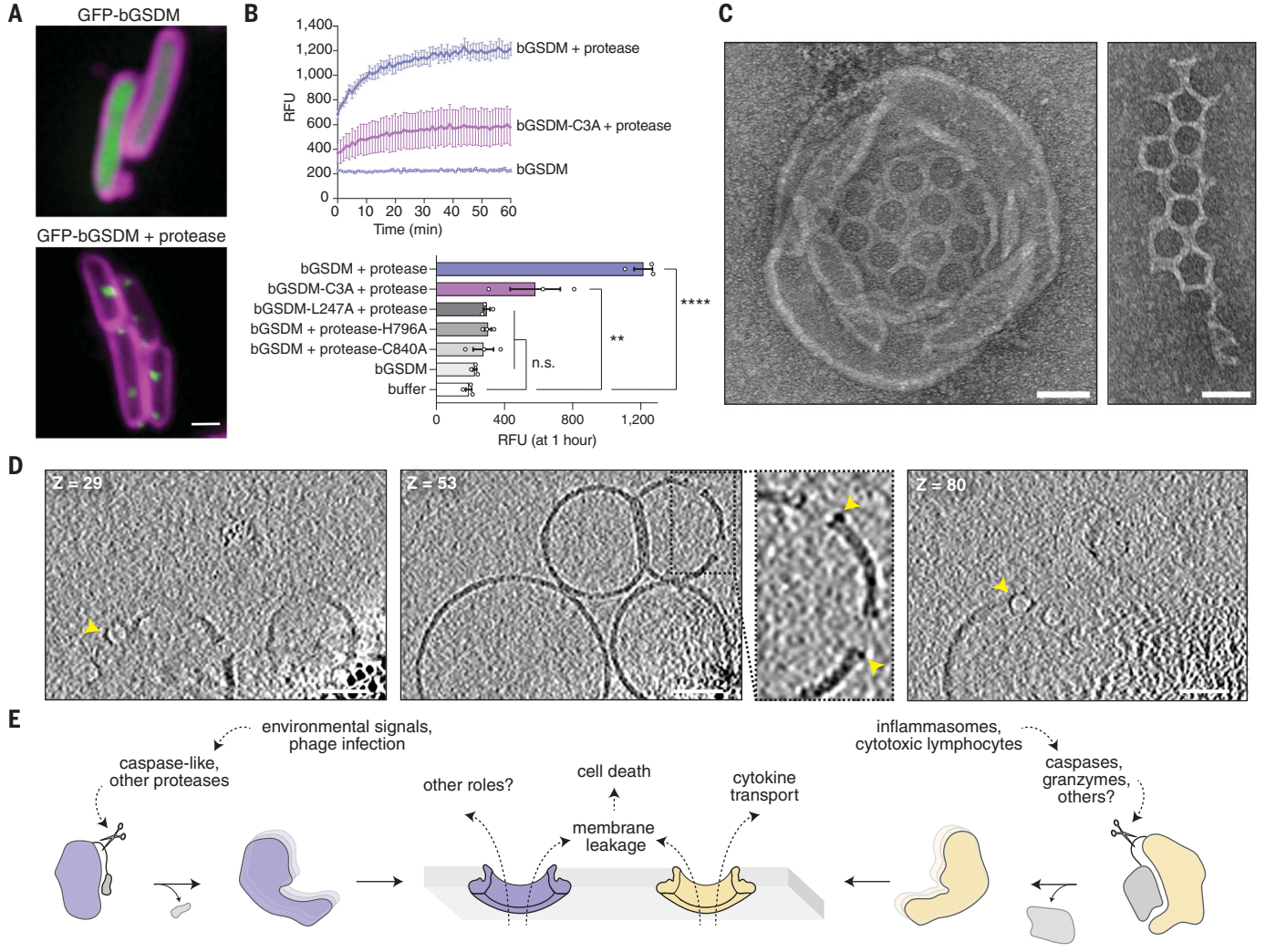

Fig. 4. Cleaved bGSDMs form membrane pores to elicit cell death. (**A**) GFP was fused to the N terminus of the *Runella* bGSDM. Cells expressing GFP-bGSDM alone (top) or with the caspase-like protease (bottom) are shown. GFP is colored green. Membrane dye (FM4-64) is in magenta. Scale bar, 1 μm. (**B**) Cleaved *Runella* gasdermin permeabilizes liposome membranes. Relative fluorescence units (RFU) were measured continuously from cleavage reactions of dioleoylphosphatidylcholine (DOPC) liposomes loaded with $TbCl_3$ with an external solution containing 20 μM dipicolonic acid (DPA). The top plot represents an example of time-course liposome leakage, whereas the bottom bar chart shows values for each condition at 60 min. Error bars represent the SEM of three technical replicates, and statistical significance was determined by one-way ANOVA and Tukey multiple comparison test. n.s. ≥ 0.05; $^{**}P$ = 0.001 to 0.01; $^{****}P$ < 0.0001. (**C**) Negative stain electron microscopy of *Runella* gasdermin pores in DOPC liposomes (left) and in mesh-like arrays (right). Scale bars, 50 nm. (**D**) Slices from representative tomogram (1 of 10) of *Runella* gasdermin pores in DOPC liposomes, at three different depths (Z). Yellow arrowheads indicate pores inserted within the liposome membrane. Scale bars, 50 nm. (**E**) Model of pyroptosis for bGSDMs and mammalian gasdermins.

and is supported by a short parallel β strand from F253 to D255. *Bradyrhizobium* bGSDM F253 latches over the palmitoyl modification, with similar hydrophobic contacts also observed in the *Runella* and *Vitiosangium* structures (fig. S10, A and B). The *Bradyrhizobium* bGSDM C-terminal peptide terminates below the strand equivalent to β2 and is supported by hydrogen bonds from R27 to the L256 backbone and N29 to E258. Truncation of the C-terminal peptide in the *Runella*, *Bradyrhizobium*, or *Vitiosangium* bGSDM constructs led to arrested cell growth, which confirms that the C-terminal peptide is required to maintain the bGSDM autoinhibition (fig. S11, A and B).

We next used mutagenesis of the *Runella* bGSDM system to define the specificity of proteolytic cleavage and bGSDM activation. In vitro, the L247 P1 position was essential for cleavage, and proteolysis was inhibited by mutations that disrupt the P1′ glycine and the P4, P3, P2, and P3′ residues (fig. S11, C and D). Likewise, mutations that disrupt the P1 and P1′ positions eliminated toxicity in vivo (fig. S11, E and F). The *Runella* protease was not capable of activating divergent bGSDMs engineered to contain the *Runella* cleavage loop, which suggests that additional contacts specify bGSDM recognition (fig. S11, G and H). Thus, like their mammalian homologs, bGSDMs are cell death effectors activated by proteolytic cleavage.

To determine whether activated bGSDMs associate with bacterial membranes, we fused green fluorescent protein (GFP) to the N terminus of the *Runella* bGSDM and visualized expression in *E. coli*. Upon coexpression with the *Runella* protease, GFP-bGSDM

coalesced into membrane-associated puncta and induced cellular toxicity (Fig. 4A and fig. S12, A to C). Transmission electron microscopy analysis of *E. coli* expressing the active *Runella* bGSDM system revealed clear disruption of membrane integrity (fig. S13, A to C). In vitro reconstituted *Runella* bGSDM activity demonstrated that cleaved *Runella* bGSDMs permeabilized liposomes and caused rapid release of the internal contents (Fig. 4B and fig. S14, A and B). Protease active-site or bGSDM cleavage-site mutations disrupted all liposome permeabilization, which confirms that proteolysis is essential for bGSDM activation (Fig. 4B and fig. S14B). Blocking bGSDM palmitoylation with mutation of residue C3 reduced but did not abolish liposome leakage or membrane-associated puncta formation in cells (Fig. 4B and fig. S12A). Likewise, a C7A mutation to the putative *Lysobacter* bGSDM palmitoylation site was not sufficient to abolish antiphage defense (fig. S8B), which suggests that lipid-modification supports but is not required for membrane permeabilization.

To compare the bGSDM pore with its mammalian counterparts, we used electron microscopy to visualize *Runella* bGSDM cleavage reactions and liposomes (Fig. 4C and fig. S15, A to C). bGSDM pores were observed within liposomes and as fragmented mesh-like arrays. Cryo–electron microscopy (cryo-EM) and two-dimensional (2D) classification analysis of detergent-solubilized complexes revealed that *Runella* bGSDM forms a ringlike pore that exhibits a width of ~50 Å and an inner diameter ranging from 200 to 300 Å (fig. S17, A to D). *Runella* bGSDM pores within liposomes measured ~240 to 330 Å—larger than the 135- to 215-Å mammalian gasdermin pores (fig. S17, A to D) (*6*, *10*, *16*). We also reconstituted cleavage of a bGSDM from a metagenomic *Bacteroidetes* scaffold and observed smaller 130- to 190-Å pores within liposomes, which suggests heterogeneity in the architecture of diverse bGSDM pores (fig. S18, A to D, and fig. S19, A to C). Cryo–electron tomography (cryo-ET) tilt series reconstructions of the pore-liposome assemblies confirmed that bGSDM pores span the liposomal surface to disrupt membrane integrity (Fig. 4D, fig. S20, and movies S3 and S4).

Our results support a model for gasdermin pore formation and effector function that has notable parallels between bacteria and mammals (Fig. 4E). bGSDM systems can exert antiphage defense, and the fusion of bGSDM-associated proteases with NACHT and repeat domains suggests that, similar to inflammasome sensors in mammals, foreign pathogen recognition may control the initiation of gasdermin cleavage (Fig. 2, B to D) (*15*, *17*). In both mammalian gasdermin and bGSDM systems, proteolytic cleavage after the lipophilic NTD releases gasdermin inhibition. The notably short C-terminal peptide responsible for bGSDM inhibition suggests the possibility that short-form eukaryotic gasdermins, including pejvakin, may undergo activation through a similar mechanism. Furthermore, widespread palmitoylation of bGSDMs indicates that cysteine modifications are a conserved mechanism for regulating gasdermin pores (*18*). The size distribution of pores from *Runella* and *Bacteroidetes* species might suggest that bGSDM pores, like those in mammals, could be customized for the secretion of certain molecules (*10*). Defining the cues that activate bGSDM systems will provide insight into their roles in prokaryotic biology and the origins of pyroptotic cell death.

REFERENCES AND NOTES

1. N. Kayagaki *et al.*, *Nature* **526**, 666–671 (2015).
2. J. Shi *et al.*, *Nature* **526**, 660–665 (2015).
3. W. T. He *et al.*, *Cell Res.* **25**, 1285–1298 (2015).
4. X. Liu *et al.*, *Nature* **535**, 153–158 (2016).
5. J. Ding *et al.*, *Nature* **535**, 111–116 (2016).
6. J. Ruan, S. Xia, X. Liu, J. Lieberman, H. Wu, *Nature* **557**, 62–67 (2018).
7. S. Jiang, Z. Zhou, Y. Sun, T. Zhang, L. Sun, *Sci. Immunol.* **5**, eabd2591 (2020).
8. J. Lieberman, H. Wu, J. C. Kagan, *Sci. Immunol.* **4**, eaav1447 (2019).
9. A. Daskalov, P. S. Mitchell, A. Sandstrom, R. E. Vance, N. L. Glass, *Proc. Natl. Acad. Sci. U.S.A.* **117**, 18600–18607 (2020).
10. S. Xia *et al.*, *Nature* **593**, 607–611 (2021).
11. Z. Liu *et al.*, *Immunity* **51**, 43–49.e4 (2019).
12. P. Broz, P. Pelegrín, F. Shao, *Nat. Rev. Immunol.* **20**, 143–157 (2020).
13. C. Clavé *et al.*, *bioRxiv* 2021.06.03.446900 [Preprint] (2021).
14. D. Kümmel, U. Heinemann, M. Veit, *Proc. Natl. Acad. Sci. U.S.A.* **103**, 12701–12706 (2006).
15. M. Shi, P. Zhang, S. M. Vora, H. Wu, *Curr. Opin. Cell Biol.* **63**, 194–203 (2020).
16. J. M. Hansen *et al.*, *Cell* **184**, 3178–3191.e18 (2021).
17. G. Kaur, A. M. Burroughs, L. M. Iyer, L. Aravind, *eLife* **9**, e52696 (2020).
18. F. Humphries *et al.*, *Science* **369**, 1633–1637 (2020).

ACKNOWLEDGMENTS

The authors thank members of the Kranzusch and Sorek laboratories for helpful discussions. Mass spectrometry was performed at the Biopolymers and Proteomics Core Facility at the Koch Institute of MIT, the Taplin Mass Spectrometry Facility at Harvard Medical School, and the Weizmann De Botton Protein Profiling Institute. We thank W. Shih's laboratory for training and use of the JEOL-1400 electron microscope, the Harvard Center for Cryo-Electron Microscopy (HC2EM), the HMS Electron Microscopy Facility, M. Eck for sharing computational resources, and the SBGrid consortium for computational support. We thank J. Leitz and A. Brunger for sharing scripts for cryo-ET reconstruction. **Funding:** This study was supported by the Pew Biomedical Scholars Program (P.J.K.), the Burroughs Wellcome Fund PATH award (P.J.K.), the Mathers Foundation (P.J.K.), the Parker Institute for Cancer Immunotherapy (P.J.K.), European Research Council grant ERC-CoG 681203 (R.S.), Israel Science Foundation grant ISF 296/21 (R.S.), the Ernest and Bonnie Beutler Research Program of Excellence in Genomic Medicine (R.S.), the Minerva Foundation and Federal German Ministry for Education and Research (R.S.), the Knell Family Center for Microbiology (R.S.), the Yotam project and the Weizmann Institute Sustainability and Energy Research Initiative (R.S.), the Dr. Barry Sherman Institute for Medicinal Chemistry (R.S.), National Institute of Health Cancer Immunology training grant T32CA207021 (A.G.J.), a Life Science Research Foundation postdoctoral fellowship of the Open Philanthropy Project (A.G.J.), a Minerva Foundation postdoctoral fellowship (T.W.), and a Herchel Smith Graduate Research Fellowship (B.D.-L.).
Author contributions: Conceptualization: A.G.J., T.W., G.A., R.S., and P.J.K. Methodology: A.G.J., T.W., M.L.M., B.D.-L., E.Y., Y.O.-S., R.S., and P.J.K. Investigation: A.G.J., T.W., M.L.M., B.D.-L., E.Y., Y.O.-S., R.S., and P.J.K. Visualization: A.G.J., T.W., and M.L.M. Funding acquisition: R.S. and P.J.K. Project administration: R.S. and P.J.K. Supervision: R.S. and P.J.K. Writing – original draft: A.G.J., T.W., R.S., and P.J.K. Writing – review and editing: A.G.J., T.W., M.L.M., B.D.-L., E.Y., Y.O.-S., G.A., R.S., and P.J.K. **Competing interests:** R.S. is a scientific cofounder and advisor of BiomX, Pantheon Bioscience, and Ecophage. The remaining authors have no competing interests to declare. **Data and materials availability:** Atomic coordinates and structure factors for the reported crystal structures have been deposited with the Protein Data Bank under accession numbers 7N50 (*Bradyrhizobium* bGSDM), 7N51 (*Vitiosangium* bGSDM), and 7N52 (*Runella* bGSDM). Correspondence and requests for other materials should be addressed to P.J.K. or R.S.

SUPPLEMENTARY MATERIALS

science.org/doi/10.1126/science.abj8432
Materials and Methods
Figs. S1 to S20
Tables S1 to S6
References (*19*–*47*)
MDAR Reproducibility Checklist
Movies S1 to S4

View/request a protocol for this paper from *Bio-protocol*.

7 June 2021; resubmitted 21 October 2021
Accepted 22 November 2021
10.1126/science.abj8432

Science

Bacterial gasdermins reveal an ancient mechanism of cell death

Alex G. JohnsonTanita WeinMegan L. MayerBrianna Duncan-LoweyErez YirmiyaYaara Oppenheimer-ShaananGil AmitaiRotem SorekPhilip J. Kranzusch

Science, 375 (6577), • DOI: 10.1126/science.abj8432

Ancient origin of cell death

Gasdermins are cell death proteins in mammals that form membrane pores in response to pathogen infection. Johnson *et al*. report that diverse bacteria encode structural and functional homologs of mammalian gasdermins. Like their mammalian counterparts, bacterial gasdermins are activated by caspase-like proteases, oligomerize into large membrane pores, and defend against pathogen—in this case, bacteriophage—infection. Proteolytic activation occurs through the release of a short inhibitory peptide, and many bacterial gasdermins are lipidated to facilitate membrane pore formation. Pyroptotic cell death, a central component of mammalian innate immunity, thus has a shared origin with an ancient antibacteriophage defense system. —SMH

Science (ISSN) is published by the American Association for the Advancement of Science. 1200 New York Avenue NW, Washington, DC 20005. The title *Science* is a registered trademark of AAAS.